

Swept source optical coherence tomography using an all-fiber 1300nm ring laser source

Michael A. Choma^{1*}, Kevin Hsu², Joseph A. Izatt¹

¹Department of Biomedical Engineering, Duke University, Durham, NC 27708

²Micron Optics, Inc. Atlanta, GA 30345

* Corresponding Author: 136 Hudson Hall, Department of Biomedical Engineering, Duke University, Durham, NC 27708. Phone: (919)660-2475. Fax: (919)660-2476.

Email: mac32@duke.edu

Abstract: The increased sensitivity of spectral domain OCT has driven the development of a new generation of technologies in OCT, including rapidly tunable, broad bandwidth swept laser sources and spectral domain OCT interferometer topologies. In this manuscript, the operation of a turnkey 1300nm swept laser source is demonstrated. This source has a fiber ring cavity with a semiconductor optical amplifier gain medium. Intracavity mode selection is achieved with an in-fiber tunable fiber Fabry-Perot filter. A novel optoelectronic technique that allows for even sampling of the swept source OCT signal in k-space also is described. A differential swept source OCT system is presented, and images of *in vivo* human cornea and skin are presented. Lastly, the effects of analog-to-digital converter aliasing on image quality in swept source OCT are discussed.

Keywords: Optical coherence tomography; Medical and biological imaging; Tunable lasers; Ophthalmic imaging; Skin imaging

1. Background and Motivation

Optical coherence tomography (OCT) is a non-contact, non-destructive imaging modality that acquires depth-resolved two- and three-dimensional images of biological tissue.¹ Since its introduction in 1991, the vast majority of OCT imaging systems have employed the principles of time domain (TD) low coherence interferometry. In low coherence interferometry, an interferometric signal is generated if and only if the pathlength of a sample reflector matches that of the scanning reference reflector. In this approach, spectral information is integrated at a single photodiode, and the interferometric signal for a single sample reflector is given by:

$$i_{\text{doct}}(x) \sim \sqrt{R_R R_S} \int_0^{\infty} S(k) \cos(2kx) dk \quad (1)$$

Here, k is optical wavenumber, x is the pathlength mismatch between the reference and sample reflectors, $S(k)$ is the source spectral density, and R_R and R_S are the reference and sample arm reflectivities, respectively. The inefficiency presented by the approach arises because, while all depths of a sample are illuminated, signal is generated in a serial manner by scanning of the reference arm. The magnitude of the inefficiency is on the order of the ratio of the scan depth Δx_{max} to the coherence length l_c , which is typically 10^2 to 10^3 . In this context, coherence length refers to the width of the axial coherence function (i.e. axial point spread function).

In 1995 Fercher, *et. al.*² proposed the use of spectral domain interferometric techniques for the generation of depth-resolved reflectivity profiles (i.e. A-scans) in scattering tissues. Two spectral domain techniques were presented. The first technique, which we call Fourier domain (FD) OCT, uses a broadband light source and collects the spectrally-resolved interference signal in a detector-arm dispersive spectrometer. The second, which we call swept

Deleted: ,

source (SS) OCT, time encodes spectral information by sweeping a narrow linewidth laser through a broad optical bandwidth. As in time domain OCT, swept source OCT uses a single photodiode detector. The detector responses for swept source and Fourier domain OCT are Eqs. (2) and (3), respectively:

$$i_{ssoct}(k) \sim \sqrt{R_R R_S} \int_k^{k+\delta k} S(k) \cos(2kx) dk \quad (2)$$

$$q_{fdoct}(k) \sim \sqrt{R_R R_S} \int_0^{1/f_{scan}} \int_k^{k+\delta k} S(k) \cos(2kx) dk dt. \quad (3)$$

The swept source OCT signal $i_{ssoct}(k)$ is a photocurrent integrated over the linewidth of the swept laser source, while the Fourier domain OCT signal $q_{fdoct}(k)$ is the quantity of photoelectrons collected over the duration of an A-scan in a charge accumulation detector such as a charge coupled device or photodiode array.

Although the initial work by Fercher, *et. al.* described the fundamental physical similarities between Fourier domain and swept source OCT, the sensitivities of spectral domain OCT compared to time domain OCT remained an open issue. In 1998 Andretzky, *et. al.*³ derived an expression for the sensitivity of Fourier domain OCT that showed its theoretical superior sensitivity to time domain OCT. This expression was later independently re-derived and experimentally verified in 1999 by Mitsui⁴ and in 2003 by Letigeb, *et. al.*⁵ and de Boer, *et. al.*⁶ These works, however, overlooked the underlying similarities between swept source and Fourier domain OCT that Fercher, *et. al.* recognized. These similarities were exploited by Choma, *et. al.*⁷ to provide a unified theoretical and experimental sensitivity analysis of all spectral domain OCT techniques that demonstrates the general sensitivity advantage of spectral domain OCT over time domain OCT. This analysis is summarized by two key points. First, the shot noise-limited signal-to-noise ration (SNR) of an individual spectral domain pixel is given by

$$\text{SNR}(k_n) = \frac{\rho}{e} P_s(k_n) R_s \Delta t \quad (4)$$

where k_n is the n^{th} wavenumber measured ($n \in [1..N]$), $P_s(k_n)$ is the sample power at k_n , R_s is the sample reflectivity, Δt is the A-scan time, ρ is the detector responsivity, and e is the electronic charge. It should be noted that each $\text{SNR}(k_n)$ is comparable to the standard time domain SNR expression given by Swanson, *et. al.*⁸ The second key point is that, while signal adds coherently during Fourier transformation from the spectral to the time domain, noise adds incoherently. This leads to a sensitivity advantage of spectral domain OCT on the order of $N \sim 10^2$ to 10^3 (Fig. 1). The SNR of spectral domain OCT is thus:

$$\text{SNR}_{\text{sdOCT}} = \frac{\rho}{2e} P_s R_s \Delta t \quad (5)$$

where P_s is the total power incident on the sample.

One of the impediments to the development of robust swept source OCT systems has been the availability of stable, rapidly tunable swept laser sources. Previously swept sources have included grating⁹ and prism¹⁰ tuned external cavity lasers and current tuning of a laser diode.¹¹ Recently, we⁷ and others¹² have demonstrated a rapidly tunable swept laser source that employs a fiber ring laser configuration with an intracavity wavelength tuning mechanism. This general cavity configuration was first demonstrated in the mid-1990s,^{13, 14} and commercial devices with an Erbium-doped fiber ring that use the fiber Fabry Perot tuning mechanism shown in this manuscript have been commercially deployed.¹⁵ In this manuscript, we describe the design and operation of a 1300nm swept source OCT system based on a modified version of this commercially-available swept laser source. We demonstrate a novel optoelectronic wavenumber linearization technique that eliminates the need for resampling spectral domain data in software.

We show high-quality SS-OCT images of the cornea and anterior segment, and discuss aliasing as a source of image artifact in spectral domain OCT.

2. Swept Source OCT System Design

A schematic of the novel all-fiber swept laser source is shown in Fig. 2. The fiber ring cavity has two important elements. First, the gain medium is a semiconductor optical amplifier that achieves population inversion via current pumping. Second, addressable wavelength (mode) selection is achieved with a fiber Fabry-Perot tunable filter (FFP-TF), a completely in-fiber device with a <2dB insertion loss. The FFP-TF is actuated by a low-voltage piezoelectric element that changes the passband of the FFP-TF by lengthening or shortening the FFP-TF. This intracavity FFP-TF has a free spectral range of 190 nm, which exceeds the gain medium bandwidth. The finesse of the FFP-TF allows tens of cavity modes to simultaneously lase within the ~0.01 nm static linewidth of the laser output.

The piezoelectric element in the FFP-TF is driven with a 250 Hz triangle wave, which generates a forward and a backward sweep. The swept laser source power as a function of wavelength and sweep direction is shown in Fig. 3. During the forward sweep, an increasing voltage ramp is applied to the piezoelectric element, which sweeps the source output from shorter to longer wavelengths. During the backward sweep, a decreasing voltage ramp is applied to the piezoelectric element, which sweeps the source output from longer to shorter wavelengths (Fig. 3). This laser achieves a 130nm sweep range centered at 1300nm, ~3mW of output power, and full-width half-maximum bandwidth of ~90nm. It should be noted that the source output is different on the forward and backward sweep. This is caused by a frequency downshift in the SOA which is believed to be due to intraband four-wave mixing via carrier-density modulation

in the SOA.¹⁶⁻¹⁸ Only the higher-intensity forward sweep was used for imaging. We have demonstrated that the sweep rate is scalable into the kilohertz regime.¹⁹

In order to achieve maximal SNR and axial imaging resolution, the digitally sampled SS-OCT data must be evenly spaced in the k-domain before Fourier transformation into an A-scan. We have implemented a novel optoelectronic method that eliminates the need for the computationally-intense software resampling needed in Fourier domain OCT. A small portion of the laser output is fed into a fixed fiber Fabry Perot interferometer (FFPI) with a free spectral range $\delta k = 372$ radians/m (17.8 GHz). The output of this FFP is monitored with a photodiode. Every time the laser sweeps through δk , the photodiode output spikes. Since these spikes are evenly spaced in wavenumber, this signal was processed in analog electronics for uses the pixel clock for analog-to-digital conversion of the interferometric signal.

Since δk is broader than the linewidth of the laser, δk determines the maximum scan depth x_{max}

$$x_{max} = \frac{1}{4 \delta k}, \quad (6)$$

The nominal noise equivalent bandwidth (NEB) of the SS-OCT system is thus⁷

$$NEB = \frac{2x_{max} \Delta \lambda}{\lambda_o} f_{ascan} = \frac{\Delta \lambda}{2 \delta \lambda} f_{ascan}, \quad (7)$$

where λ_o is the center wavelength, $\Delta \lambda$ is the laser sweep bandwidth, $\delta \lambda$ is δk expressed in wavelength, and f_{ascan} is the A-scan line rate. Due to nonlinearities in the wavenumber scan, the actual NEB will be greater than that given by Eq. (7). In other words, since the FFPI-based

trigger forces even sampling in wavenumber, it necessarily forces uneven sampling in time when the source wavenumber sweep is nonlinear. Since the *NEB* is inversely proportional to the analog-to-digital sampling interval, nonlinear sampling in time increases the *NEB* due to the presence of sampling intervals shorter than those assumed in Eqs. 6 and 7. This broadening degrades the system SNR, and is analogous to the broadening observed when a sinusoidal resonant scanner is used in a rapid scanning optical delay line in a time domain OCT system.²⁰

Our system schematic is shown in Fig. 4. The interferometer employs dual balanced detection²¹, which allows for the hardware removal of non-interferometric and autocorrelation terms. The measured system sensitivity was 119dB, which compares well with the theoretical SNR of 121dB. With $\delta\lambda=0.1\text{nm}$, the imaging scan depth was 4.2mm. The measured coherence length (i.e. axial resolution) was $9.1\mu\text{m}$ ($6.5\mu\text{m}$) in air (tissue), and the coherence length remained constant throughout the entire 4.2mm scan depth (Fig. 5). Further, the amplitude falloff at 4.2mm was $\sim 3\text{dB}$ owing to the anti-aliasing filter. Each x-domain A-scan contains 649 points.

3. *In Vivo* Swept Source OCT Imaging

We performed *in vivo* imaging of the human cornea and anterior segment using slit-lamp biomicroscope adapted optics. Details of this setup are in Patil, *et. al.*²² The image in Fig. 6 contains 300 A-scans. Major anatomic features were visualized, including the iris stroma, iris pigment epithelium, ciliary body, angle of anterior chamber, aqueous, corneal stroma, sclera, and scleral spur. The corneal epithelium was visualized in Fig. 8. A hand-held probe was used to perform imaging of the *in vivo* human skin pad. Details of the hand-held probe design are in

Radhakrishnan, *et. al.*²³ The image in Fig. 7 contains 500 A-scans. The dermis, dermal-epidermal junction, and stratum corneum were well-visualized.

Deleted:
Deleted:

4. Aliasing Artifact In Spectral Domain OCT

There have been two widely discussed sources of artifact and ambiguity in spectral domain OCT, complex conjugate ambiguity and DC artifacts. The first, complex conjugate ambiguity, arises because reflectors at $+x$ are superimposed over those at $-x$, owing to the fact that the spectral domain signal is real-valued. Complex conjugate ambiguity also reduces the laser linewidth (or spectrometer resolution) limited scan depth by a factor of two. The second source of artifact arises because autocorrelation and source spectral shape terms are centered around $x=0$. A third source of ambiguity arises when spectral domain fringes from depths greater than x_{max} are aliased down to depths less than x_{max} (Fig. 8). The apparent or aliased depth of an object x_a is given by:

$$x_a = \begin{cases} \text{mod}(x, 2x_{max}) & \text{if } \text{mod}(x, 2x_{max}) \leq x_{max} \\ x_{max} - \text{mod}(x, 2x_{max}) & \text{if } \text{mod}(x, 2x_{max}) > x_{max} \end{cases}, \quad (8)$$

where $\text{mod}(a,b)$ yields a modulo b . This phenomenon has been discussed in Fourier transform spectral interferometry²⁴, and a similar effect occurs in magnetic resonance imaging.²⁵ Aliasing can be mitigated by passing the photodetector output through the noise equivalent bandwidth-limiting anti-aliasing filter (Fig. 4).⁷ Aliasing is a difficult problem to eliminate because analog filters have finite impulse response transfer functions and, as such, cannot act as a perfect brickwall filters with a cutoff frequency corresponding to the system noise equivalent bandwidth dictated by x_{max} . Doubling the scan depth through by resolving complex conjugate ambiguity

reduces the likelihood of aliasing. Oversampling and subsequent processing with an infinite impulse response digital filter is another potential solution.

5. Conclusions

In conclusion, we have presented a swept source OCT system with an all-fiber, turnkey swept laser source. We demonstrated a novel optoelectronic wavenumber linearization technique that yielded a near-transform-limited point spread function performance over the entire scan range, which had not previously been convincingly demonstrated with either Fourier domain or swept source OCT. We obtained excellent *in vivo* images of the human cornea and anterior segment, and are currently scaling this system into the kilohertz regime for real time imaging.

6. Acknowledgements

This work was supported by National Institutes of Health grant R24-EB000243.

7. References

1. D. Huang, E. A. Swanson, C. P. Lin, J. S. Schuman, W. G. Stinson, W. Chang, M. R. Hee, T. Flotte, K. Gregory, C. A. Puliafito, and J. G. Fujimoto, "Optical coherence tomography.," *Science* **254**(5035), 1178-1181 (1991).
2. A. F. Fercher, C. K. Hitzenberger, G. Kamp, and S. Y. Elzaiat, "Measurement of Intraocular Distances by Backscattering Spectral Interferometry," *Optics Communications* **117**(1-2), 43-48 (1995).
3. P. Andretzky, M. W. Lindner, J. Herrmann, A. Schutz, M. Konzog, F. Kieseewetter, and G. Hausler, "Optical coherence tomography by "spectral radar," dynamic range estimation and *in vivo* measurements of skin," presented at the SPIE, 1998.

4. T. Mitsui, "Dynamic range of optical reflectometry with spectral interferometry," *Japanese Journal of Applied Physics Part 1-Regular Papers Short Notes & Review Papers* **38**(10), 6133-6137 (1999).
5. R. Leitgeb, C. K. Hitzenberger, and A. F. Fercher, "Performance of fourier domain vs. time domain optical coherence tomography," *Optics Express* **11**(8), 889-894 (2003).
6. J. F. de Boer, "Signal to noise gain of spectral domain over time domain optical coherence tomography," presented at the Photonics West, San Jose, January 2004, 2004.
7. M. A. Choma, M. V. Sarunic, C. Yang, and J. A. Izatt, "Sensitivity advantage of swept-source and Fourier-domain optical coherence tomography," *Optics Express* **11**(18), 2183-2189 (2003).
8. E. A. Swanson, D. Huang, M. R. Hee, J. G. Fujimoto, C. P. Lin, and C. A. Puliafito, "High-Speed Optical Coherence Domain Reflectometry," *Optics Letters* **17**(2), 151-153 (1992).
9. S. R. Chinn, E. A. Swanson, and J. G. Fujimoto, "Optical coherence tomography using a frequency-tunable optical source," *Optics Letters* **22**(5), 340-342 (1997).
10. B. Golubovic, B. E. Bouma, G. J. Tearney, and J. G. Fujimoto, "Optical frequency-domain reflectometry using rapid wavelength tuning of a Cr⁴⁺:forsterite laser," *Optics Letters* **22**(22), 1704-1706 (1997).
11. U. H. P. Haberland, V. Blazek, and H. J. Schmitt, "Chirp Optical Coherence Tomography of Layered Scattering Media," *Journal of Biomedical Optics* **3**(3), 259-266 (1998).
12. S. H. Yun, G. J. Tearney, J. F. de Boer, N. Iftimia, and B. E. Bouma, "High-speed optical frequency-domain imaging," *Optics Express* **11**(22), 2953-2963 (2003).

13. H. Porte, T. Frison, P. Mollier, and J. P. Doedgebuer, "Electrooptic tuning of a fiber ring semiconductor laser," *IEEE Photonics Technology Letters* **7**, 700-702 (1995).
14. D. Y. Zhou, P. R. Prucnal, and I. Glesk, "A widely tunable narrow linewidth semiconductor fiber ring laser," *Ieee Photonics Technology Letters* **10(6)**, 781-783 (1998).
15. K. Hsu, P. J. Santangelo, and S. Y. Set, "Swept-wavelength laser measurement systems enable real-time monitoring and in-process control during optical manufacturing," presented at the The 6th World Multiconference on Systemics, Cybernetics and Informatics (SCI'2002), 2002.
16. S. H. Yun, C. Boudoux, M. C. Pierce, J. F. de Boer, G. J. Tearney, and B. E. Bouma, "Extended-cavity semiconductor wavelength-swept laser for biomedical imaging," *IEEE Photonics Technology Letters* **16(1)**, 293-295 (2004).
17. G. P. Agrawal, "Population Pulsations and Nondegenerate 4-Wave Mixing in Semiconductor-Lasers and Amplifiers," *Journal of the Optical Society of America B-Optical Physics* **5(1)**, 147-159 (1988).
18. K. Inoue, T. Mukai, and T. Saitoh, "Nearly Degenerate 4-Wave-Mixing in a Traveling-Wave Semiconductor-Laser Amplifier," *Applied Physics Letters* **51(14)**, 1051-1053 (1987).
19. K. Hsu, T. Haber, J. Mock, J. Volcy, and T. W. Graver, "High-speed swept-laser interrogation system for vibrational monitoring," presented at the International Workshop on Structure Health Monitoring 2003 (IWSHM4), Sep.15-17, 2003, 2003.
20. A. M. Rollins, M. D. Kulkarni, S. Yazdanfar, R. Ung-arunyawee, and J. A. Izatt, "In vivo video rate optical coherence tomography," *Optics Express* **3(6)**, 219-229 (1998).

21. A. M. Rollins and J. A. Izatt, "Optimal interferometer designs for optical coherence tomography," *Optics Letters* **24**(21), 1484-1486 (1999).
22. C. A. Patil, B. A. Bower, V. Westphal, S. W. Jeon, A. M. Rollins, Y. Li, D. Huang, and J. A. Izatt, "Slit-lamp adapted, video-correlated real-time optical coherence tomography of the anterior segment," presented at the Advances in Optical Imaging and Photon Migration, OSA Topical Meeting, Miami Beach, Florida, 2002.
23. S. Radhakrishnan, A. M. Rollins, J. E. Roth, S. Yazdanfar, V. Westphal, D. S. Bardenstein, and J. A. Izatt, "Real-time optical coherence tomography of the anterior segment at 1310 nm," *Archives of Ophthalmology* **119**(8), 1179-1185 (2001).
24. C. Dorrer, N. Belabas, J. P. Likforman, and M. Joffre, "Spectral resolution and sampling issues in Fourier-transform spectral interferometry," *Journal of the Optical Society of America B-Optical Physics* **17**(10), 1795-1802 (2000).
25. A. L. Horowitz, *MRI Physics for Radiologists : A Visual Approach*, 3rd edition ed. (Springer-Verlag, New York, 1995), p. 192.

Figures and Captions

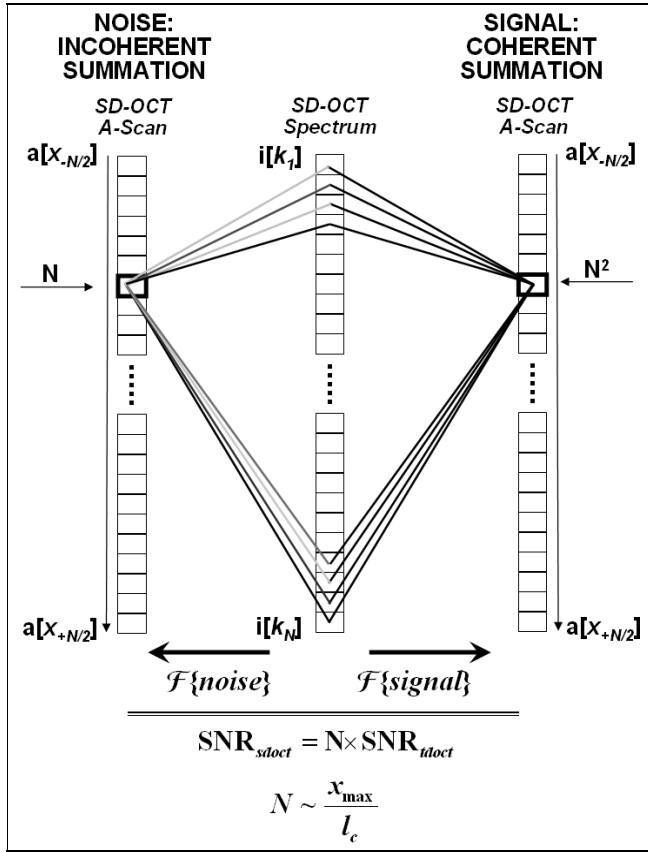


Figure 1. Sensitivity advantage of spectral domain OCT. Each pixel of the SD-OCT signal $i[k_n]$ has an SNR comparable to that of an entire TD-OCT A-scan. When $i[k_n]$ is Fourier transformed to retrieve the depth-resolved A-scan, the signal adds coherently, while the noise adds incoherently, yielding an SNR that is N times greater than the k-domain pixel SNR. Further, N is proportional to the ratio of the scan depth x_{max} and the source coherence length l_c . In this context, coherence length refers to the width of the axial coherence function (i.e. axial point

spread function). The grayscale intensity of the lines drawn from the spectral to the time domain represents the relative phase of the Fourier components.

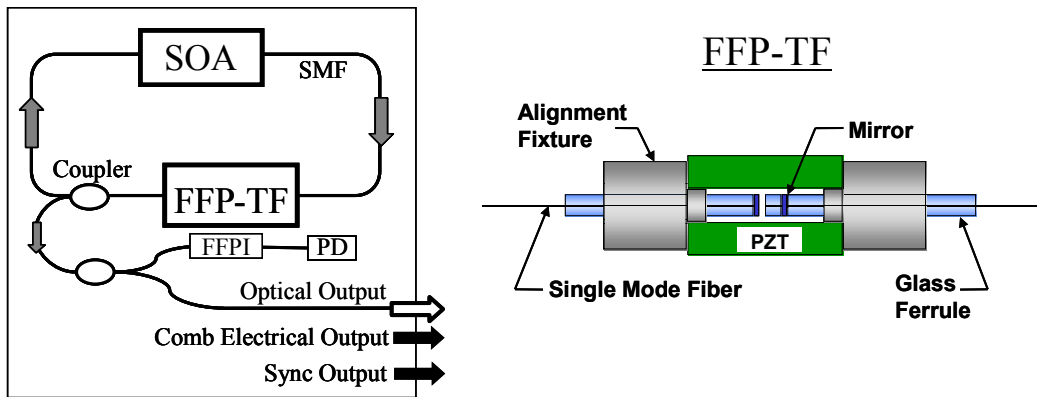


Figure 2. Right: Schematic of 1300nm swept laser source. Addressable cavity mode selection is performed by the fiber Fabry-Perot tunable filter (FFP-TF). A small portion of the laser output is fed to a fixed fiber Fabry Perot interferometer (FFPI), which is monitored by a photodiode (PD). The electrical comb output of this photodiode serves as the pixel clock for the analog-to-digital converter. SMF: single-mode fiber, SOA: semiconductor optical amplifier. Left: Schematic of FFP-TF. PZT: piezoelectric tuning element.

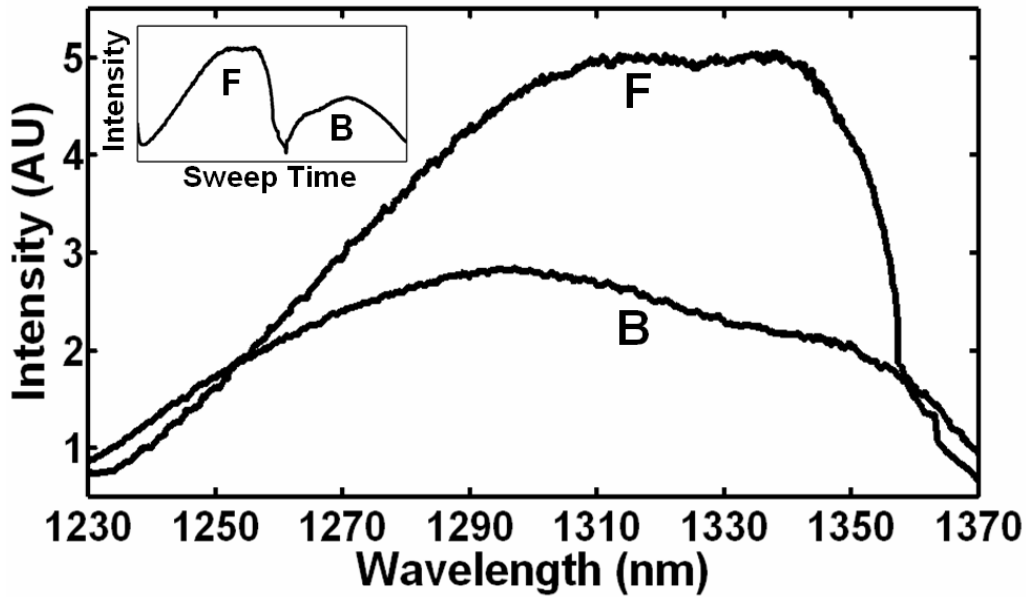


Figure 3. Output spectrum of swept laser source. The piezoelectric element in the FFP-TF is driven with a triangle wave, which generates a forward (F) and a backward (B) sweep. During the forward sweep, an increasing voltage ramp is applied to the piezoelectric element, which sweeps the source output from shorter to longer wavelengths. During the backward sweep, a decreasing voltage ramp is applied to the piezoelectric element, which sweeps the source output from longer to shorter wavelengths. The source intensity as a function of time is shown in the inset. This recording was evenly sampled in wavenumber using the pixel trigger mechanism described in Figure 4 and in Section 2 of the text. By using the minimum and maximum source wavelengths measured using an optical spectrum analyzer, the intensity versus time recording was replotted as intensity versus wavelength.

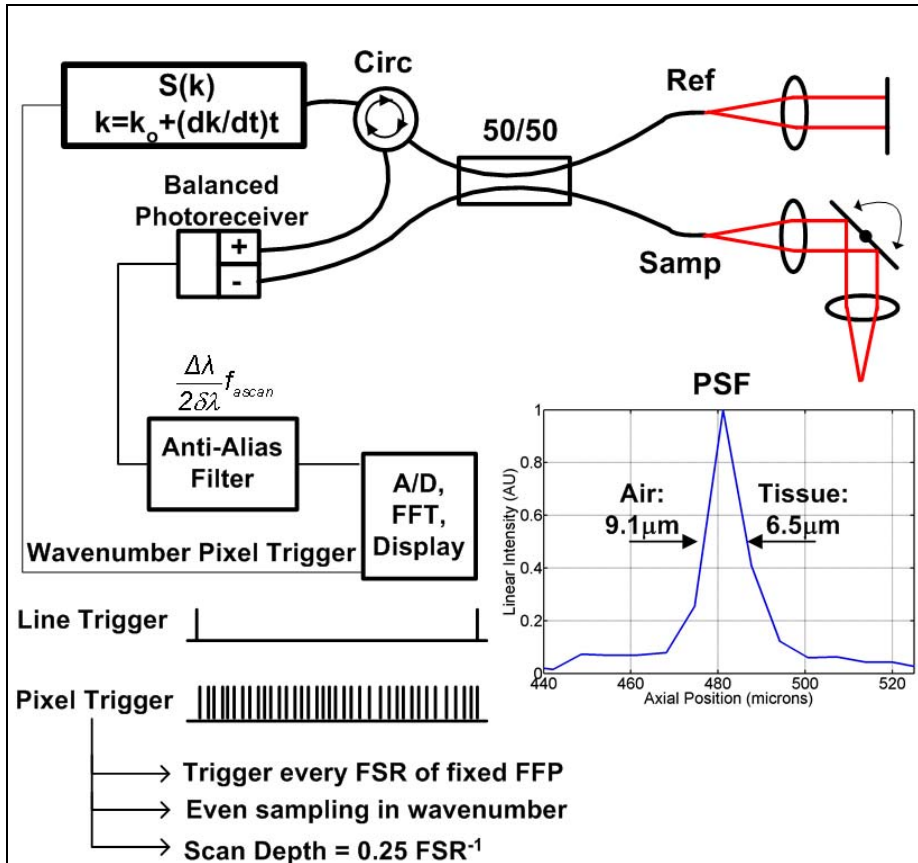


Figure 4. Schematic of the SS-OCT imaging system. The source sweep function $S(k)$ (k , optical wavenumber) is parametrized by time with the expression $k = k_0 + (dk/dt)t$, where k_0 is the wavenumber at $t=0$ and t is taken modulo the total sweep time. The interferometer employs dual balanced detection, which allows for the hardware removal of non-interferometric and autocorrelation terms. An anti-aliasing filter sets the system noise equivalent bandwidth and mitigates the effect of high-frequency interferometric (i.e. structural) information aliased to lower frequencies. The analog-to-digital converter has two trigger inputs. The first is a line trigger, provided by the function generator that drives the intracavity fiber Fabry-Perot tunable

filter. The second is a pixel clock generated by a photodetector that monitored the output of a fixed fiber Fabry-Perot interferometer that is fed a small portion of the laser output. Every time the source sweeps through the free spectral range of the FFP-I, the photodetector output spikes, and a sample is taken by the A/D. This allows for even sampling of the signal in k-space. Since the free spectral range of the FFP-I is 372 radians/m (17.8 GHz), each linescan consists of 1298 samples. The axial point spread function (PSF) of the SS-OCT system had a full-width half-maximum of 9.1 μ m in air and 6.5 μ m in tissue.

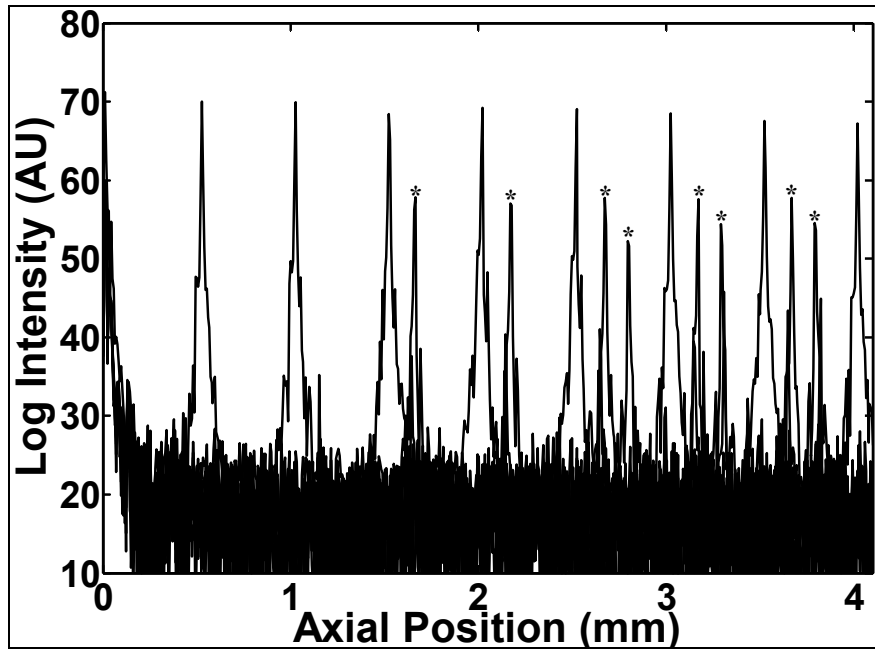


Figure 5. A-scans of a calibrated reflector taken at 0.5 mm increments over a 4.2 mm scan depth. The falloff in peak intensity from 0 to 4.2 mm was ~ 3 dB. Further, there was no increase in peak width over the scan range. Each A-scan contains 649 pixels. Peaks marked with a ‘*’ are echoes from a neutral density filter in the reference arm.

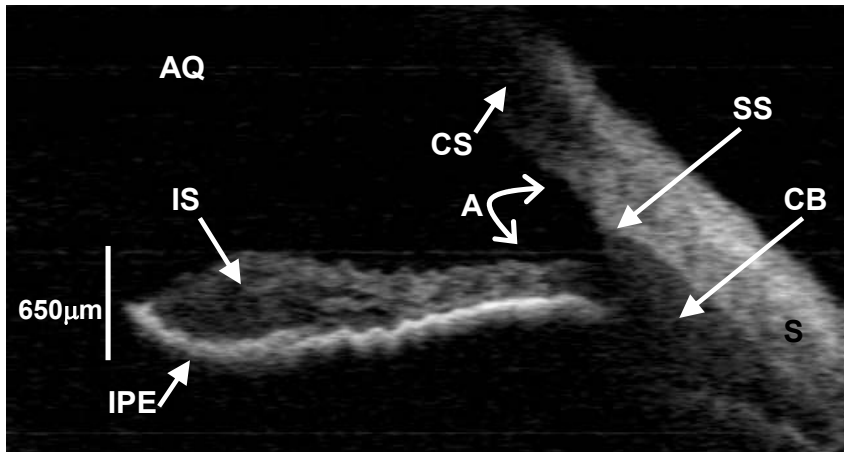


Figure 6. SS-OCT image of cornea angle region. Note the significant contrast between the iris stroma (IS) and the iris pigment epithelium (IPE), as well as the sharply defined ciliary body (CB). The image contains 300 A-scans. A: Angle of anterior chamber, AQ: aqueous, CS: corneal stroma, S: sclera, SS: scleral spur.

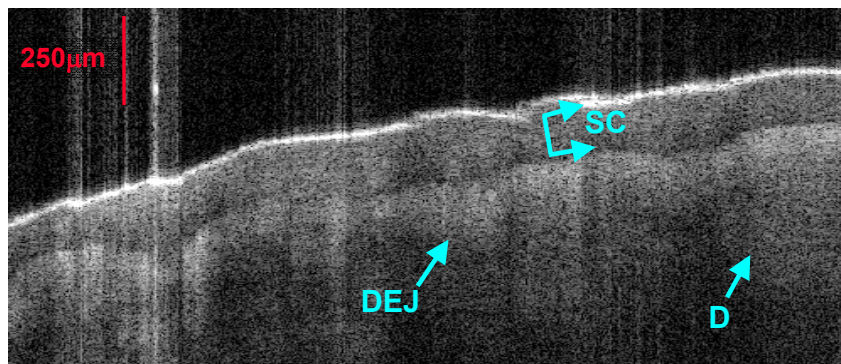


Figure 7. Swept source OCT image of fingerpad. The bright lines on the lefthand side of the figure are artifact due to detector saturation. The image contains 500 A-scans. D, dermis; DEJ, dermal-epidermal junction, SC, stratum corneum.

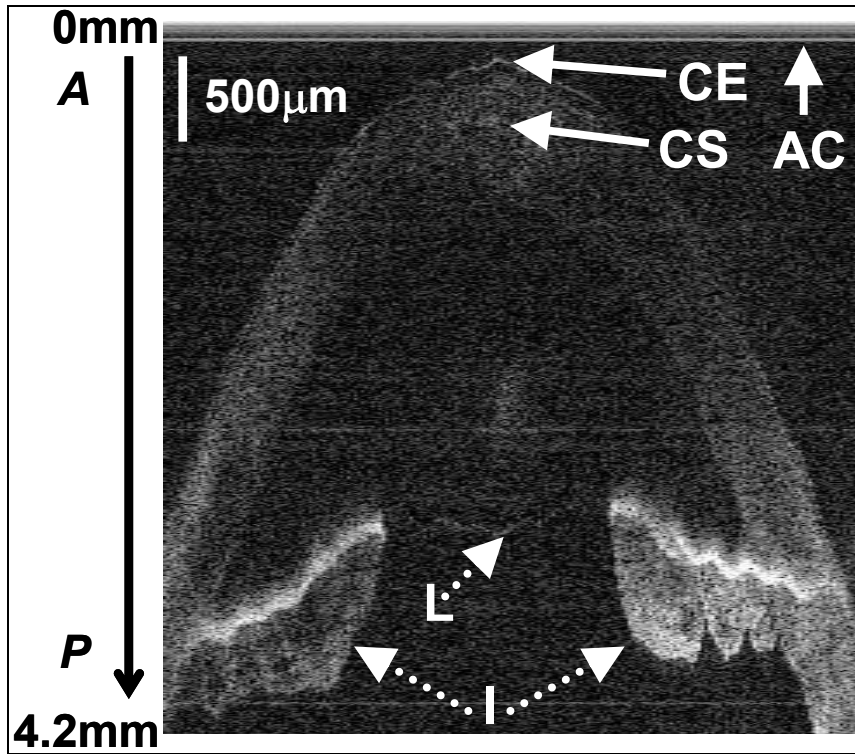


Figure 8. Effect of aliasing on imaging the cornea and anterior segment. Aliased features are noted by dashed arrows, and *A* and *P* denote anterior and posterior, respectively. The irides (I) and lens (L) are anatomically posterior to termination of the 4.2mm scan, but they are aliased anterior to this termination. Furthermore, aliasing creates mirror images of the irides and lens around the posterior border of the image, consistent with Eq. (8). AC, autocorrelation and spectral shape terms; CE, corneal epithelium, CS, corneal stroma